10th World Congress on Structural and Multidisciplinary Optimization
May 19 - 24, 2013, Orlando, Florida, USA

Optimization of Bistable Viscoelastic Systems

Kristian E. Jensen[1], Peter Szabo[2], Fridolin Okkels[3]

[1] Technical University of Denmark, Copenhagen, Denmark, kristian.jensen@nanotech.dtu.dk
[2] Technical University of Denmark, Copenhagen, Denmark, ps@kt.dtu.dk
[3] Technical University of Denmark, Copenhagen, Denmark, fridolin.okkels@nanotech.dtu.dk

1. Abstract
We consider the flow of a viscoelastic fluid in a symmetric cross geometry. For small driving pressures the flow is symmetric, but beyond a certain critical pressure the symmetric flow becomes unstable; two stable asymmetric solutions appear, and forcing of the unstable symmetric flow beyond the critical pressure gives rise to increased hydraulic resistance. We have combined a state-of-the-art implementation for viscoelastic flow modeling with topology optimization in a high level finite element package (COMSOL). We use this framework on the cross geometry with the aim to reduce the critical driving pressure corresponding to the point of bistability, such that the effect is enhanced. The point of bistability is, however, not explicitly contained in the solution, so we opt for a heuristic approach based on the dissipation ratio between the asymmetric and unstable symmetric flow solutions. We find a solution that significantly reduces the driving pressure required for bistability, and furthermore is in agreement with the approach followed by experimental researchers. Finally, by comparing the the two asymmetric solutions, we succesfully apply the same approach to a problem with two fluids meeting in the cross.
2. Keywords: viscoelastic, bistable, topology, optimization, COMSOL.

3. Introduction

Viscoelastic fluids appear in many industrial applications due to the presence of biological components and synthetic polymers, e.g. food and plastic processing respectively. The elastic character of these small constituents can cause large normal stresses which in turn can give rise to exceptional flow phenomena such as rod climbing, upstream recirculation and bistability. Differential constitutive equations are not only able to reproduce most of these phenomena, but also provide a good quantitative agreement with experiments [2]. We have showed that recent reformulations [8] have improved the robustness of these models to the extent that they can be combined with a high-level implementation of topology optimization [13]. We used the combination to find a novel material layout for a viscoelastic rectifier [7] and verified the performance experimentally [11]. Lately we have applied optimization implementation to the cross geometry, and this paper is dedicated to these results.

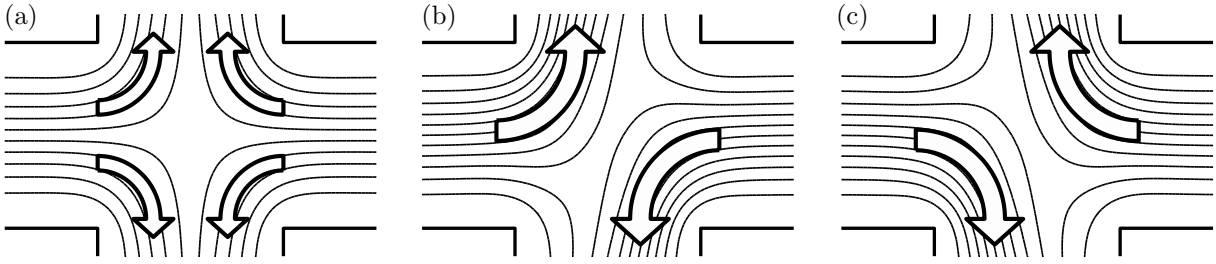

Figure 1: The viscoelastic flow in a cross is symmetric in the regime of low elasticity (a), but this becomes unstable in the regime of moderate elasticity. Instead two asymmetric solutions appear (b) and (c).

When a viscoelastic fluid flows in a cross geometry, large normal stresses arises as the fluid flows out the two side channels, see figure 1. The system lends itself to be described by a pitchfork bifurcation in the sense that the symmetric flow is stable in the low elasticity regime, while it becomes unstable and two asymmetric stable solutions appear in the regime of moderate elasticity. This phenomena of flow bistability has been observed experimentally [1] and numerically reproduced [14]. The unstable symmetric solution was investigated in simulations, which revealed that the asymmetric flow corresponds to a lower hydraulic resistance. We use this observation to formulate a heuristic objective function that allows for

minimization of the driving pressure at which bistability occurs. The heuristic approach is successful in the sense that the ideas of experimental researchers is reproduced [10], so we attempt to use the same approach for breaking the symmetry of the design. This is successful for a simple case, but validation and understand becomes more tricky for a more advanced problem.

4. Modeling

The elastic behavior of viscoelastic flow is often modeled using a statistical ensemble of flexible dumbbells (that is two point masses connected by a spring) in what is collectively referred to as dumbbell models. The end-to-end vector, $\mathbf{a}$ of such a dumbbell describes orientation as well as extension, and it defines the conformation tensor,

$$\underline{\underline{\mathbf{A}}} = \langle \mathbf{a} \otimes \mathbf{a} \rangle / \mathrm{a}_{\mathrm{eq}}^2, \tag{1}$$

where $\langle \cdots \rangle$ is a statistical average, and a_{eq} is the equilibrium length of the end-to-end vector.

Balance of stress is guaranteed by the Stokes equation

$$\rho \frac{D\mathbf{v}}{Dt} = \boldsymbol{\nabla} \cdot \left(-p\underline{\underline{\mathbf{I}}} + \eta_s \left[\boldsymbol{\nabla}\mathbf{v} \left(\boldsymbol{\nabla}\mathbf{v} \right)^T \right] + \underline{\underline{\boldsymbol{\tau}}}_e \right) - \alpha \mathbf{v} \tag{2}$$

$$0 = \boldsymbol{\nabla} \cdot \mathbf{v}, \tag{3}$$

where ρ is the density, D is the material derivative, $\mathbf{v}$ is velocity, p is pressure, $\underline{\underline{\mathbf{I}}}$ is the identity matrix and η_s is the solvent viscosity. The damping term, $-\alpha\mathbf{v}$ is used by the optimization. It vanishes in fluid regions, while solid regions are characterized by a large inverse permeability, $\alpha_{\max}$ similar to a sponge with low permeability. The polymer stress tensor $\underline{\underline{\boldsymbol{\tau}}}_e$ describes the stress due to the elastic dumbbells,

$$\underline{\underline{\boldsymbol{\tau}}}_e = \frac{\eta_p}{\lambda} k(\underline{\underline{\mathbf{A}}}) \left(\underline{\underline{\mathbf{A}}} - \underline{\underline{\mathbf{I}}} \right) \tag{4}$$

$$k(\underline{\underline{\mathbf{A}}}) = \frac{1}{1 - \mathrm{Trace}(\underline{\underline{\mathbf{A}}})/\mathrm{a}_{\max}^2}, \tag{5}$$

where η_p is the polymer viscosity, λ is the dumbbell relaxation time and $k(\underline{\underline{\mathbf{A}}})$ is a non-linear modification of the dumbbell spring constant, which constrains the trace of the conformation tensor at $\mathrm{a}_{\max}^2$ from above. Finally there is the evolution equation for the conformation tensor, which involve convection on the left-hand side and relaxation together with orientation and stretching on the right-hand side,

$$\frac{D\underline{\underline{\mathbf{A}}}}{Dt} = -\frac{k(\underline{\underline{\mathbf{A}}})}{\lambda} \left(\underline{\underline{\mathbf{A}}} - \underline{\underline{\mathbf{I}}} \right) + \left[\underline{\underline{\mathbf{A}}} \cdot \boldsymbol{\nabla}\mathbf{v} + \left(\boldsymbol{\nabla}\mathbf{v} \right)^T \cdot \underline{\underline{\mathbf{A}}} \right]. \tag{6}$$

Note how the relaxation term will tend to dominate the equation as the trace of the conformation tensor approaches $\mathrm{a}_{\max}^2$. Equations (2-6) constitute the FENE-CR model [6], which has a constant shear viscosity. This is contrary to the FENE-P model [3], which exhibit shear thinning behavior and inspired the FENE-CR model. When the FENE-CR model is analyzed with the finite element method, the velocity components are usually taken as 2nd order Lagrange polynomials with C^0 continuity, but this causes discontinuity of the velocity gradients, $\boldsymbol{\nabla}\mathbf{v}$. This can be solved by introducing a continuous approximation, $\underline{\underline{\mathbf{G}}}$ for use in equation (6). Furtheremore small solvent viscosity can cause the Navier-Stokes equation (2) to lose its elliptic character and therefore $0 = \eta_p(\underline{\underline{\mathbf{G}}} + \underline{\underline{\mathbf{G}}}^T - \boldsymbol{\nabla}\mathbf{v} - (\boldsymbol{\nabla}\mathbf{v})^T)$ is added on the right-hand [9]. Finally equation (6) can be reformulated [8] such that it is the logarithm of the conformation tensor, $\underline{\underline{\mathbf{s}}}$ that is convected. This ensures that the conformation tensor $\underline{\underline{\mathbf{A}}} = e^{\underline{\underline{\mathbf{s}}}}$ remains positive definite, which improves robustness.

Although we would like to applaud the general progress within modeling of viscoelastic fluids in complex geometries, we would also like to stress that the models remain computationally intensive due to the presence of two tensor variables. This means that state-of-the-art 3D simulations are carried out on supercomputers and even then only in simple benchmark geometries [5, 16]. Furthermore computations in the regime of high viscoelasticity is limited by the presence of small time and length scale in what is collectively referred to as viscoelastic turbulence. Presently no viscoelastic turbulence models exists. The results presented in the following are thus limited to steady 2D flow in the regime of low to moderate viscoelasticity.

We use SUPG stabilization to handle the convection-reaction equations (6) in the sense that we multiply with $\underline{\underline{\mathbf{s}}}_{\mathrm{test}} + h_{\mathrm{mesh}}(\boldsymbol{\nabla}\underline{\underline{\mathbf{s}}}_{\mathrm{test}} \cdot \mathbf{v})$ rather than just $\underline{\underline{\mathbf{s}}}_{\mathrm{test}}$, when we convert to the weak formulation.

We find a steady solutions by

#1 finding the solution corresponding to Stokes flow and setting $\underline{\underline{\mathbf{s}}} \approx \underline{\underline{\mathbf{0}}}$.

#2 initializing a transient solver with #1 and evolving for many relaxation times.

#3 initializing a static solver with #2.

We use 2nd order polynomials for $\mathbf{v}$ and 1st order for p, $\underline{\underline{\mathbf{G}}}$, $\underline{\underline{\mathbf{s}}}$ and $\underline{\underline{\mathbf{T}}}$, which is standard choice within modeling of viscoelastic fluids [5]. Finally there is a variable, θ which is discontinuous as it takes a constant value in every element. This is related to the topology optimization as explained in the section following the dimensional analysis of the governing equations.

5. Dimensionless Modeling

The FENE-CR model can be written in terms of the dimensionless variables $\tilde{x}$, $\tilde{v}$, $\tilde{t}$, $\tilde{p}$, $\underline{\underline{\tilde{\tau}}}_e$ and $\tilde{\alpha}$

$$\mathbf{x} = L_{\text{char}}\tilde{\mathbf{x}}, \quad \mathbf{v} = \frac{p_{\text{char}}L_{\text{char}}}{\eta_s+\eta_p}\tilde{\mathbf{v}}, \quad t = \frac{\eta_s+\eta_p}{p_{\text{char}}}\tilde{t}, \quad p = p_{\text{char}}\tilde{p}, \quad \underline{\underline{\tau}}_e = p_{\text{char}}\underline{\underline{\tilde{\tau}}}_e \quad \text{and} \quad \alpha = \alpha_{\max}\tilde{\alpha},$$

where we have chosen to define a characteristic velocity in terms of characteristic pressure, p_{char} rather than the other way around. This yields

$$\begin{aligned}
0 &= \tilde{\boldsymbol{\nabla}}\cdot\left(-\underline{\underline{\mathbf{I}}}\tilde{p} + \beta\left[\tilde{\boldsymbol{\nabla}}\,\tilde{\mathbf{v}} + \left(\tilde{\boldsymbol{\nabla}}\,\tilde{\mathbf{v}}\right)^T\right] + \underline{\underline{\tilde{\tau}}}_e\right) - \text{Da}^{-1}\tilde{\alpha}\tilde{\mathbf{v}}, \\
\frac{D\underline{\underline{\mathbf{A}}}}{D\tilde{t}} &= -\frac{k(\underline{\underline{\mathbf{A}}})}{\text{We}}\left(\underline{\underline{\mathbf{A}}} - \underline{\underline{\mathbf{I}}}\right) + \left[\underline{\underline{\mathbf{A}}}\cdot\tilde{\boldsymbol{\nabla}}\,\tilde{\mathbf{v}} + \left(\tilde{\boldsymbol{\nabla}}\,\tilde{\mathbf{v}}\right)^T\cdot\underline{\underline{\mathbf{A}}}\right] \\
\underline{\underline{\tilde{\tau}}}_e &= \frac{1-\beta}{\text{We}}k(\underline{\underline{\mathbf{A}}})\left(\underline{\underline{\mathbf{A}}} - \underline{\underline{\mathbf{I}}}\right) \quad \text{and} \quad k(\underline{\underline{\mathbf{A}}}) = \frac{1}{1+\text{Trace}(\underline{\underline{\mathbf{A}}})/L^2},
\end{aligned}$$

where the following characteristic physical parameters have been introduced

$$\begin{aligned}
\text{We} &= \frac{\{\text{elastic effects}\}}{\{\text{viscous effects}\}} = \frac{\lambda\Delta p}{\eta_s+\eta_p} = 0.75, \\
\beta &= \frac{\{\text{viscous effects due to solvent}\}}{\{\text{total viscous effects}\}} = \frac{\eta_s}{\eta_s+\eta_p} = 0.2, \quad a^2_{\max} = 100 \quad \text{and} \quad \Delta p = 67.2p_{\text{char}}. \quad (7)
\end{aligned}$$

These physical non-dimensional parameters represents the relative magnitude of the of the quantities between curly brackets. Note that a Newtonian fluid is recovered in the limit of We going to zero or β going to 1. Typical values of the physical parameters are listed in equation (7), while numerical parameters such as the Darcy number, Da are treated in the following section.

5. Topology Optimization

We are interested in optimizing devices relying on viscoelastic effects, but it is well known that the magnitude of viscoelastic effects increases at small length scales and the very nature of our optimization problems thus has the potential to result in designs with length scales identical to the that of the numerical discretization. This entails not only poor, if not unphysical, numerical approximation of the governing equation, but also risk of unsteady flow, the presence of which cannot be handled by the applied optimization implementation. Consequently we wish to impose a lower bound $L_{\min}$ on the length scale of the design variable, θ, and this can be achieved by using the PDE filter [12] to compute the filtered design variable, $\tilde{\theta}$. We use 2nd order Lagrange polynomials to represent $\tilde{\theta}$. The filter design unfortunately also gives rise to larger areas of intermediate material and therefore we use a projection function [19], before applying the usual convex relation [4].

$$\tilde{\theta} = \theta + L^2_{\min}\boldsymbol{\nabla}^2\tilde{\theta} \quad (8)$$

$$\bar{\theta} = \tfrac{1}{2} + \frac{\tanh(\xi(\tilde{\theta}-\tfrac{1}{2}))}{2\tanh(\xi/2)} \quad (9)$$

$$\alpha = \alpha_{\max}\frac{q(1-\bar{\theta})}{\bar{\theta}+q} \quad (10)$$

where ξ and q determines the steepness of the projection and convexity of the inverse permeability in the projected design variable, $\bar{\theta}$. Ideally ξ, $\alpha_{\max}$ and q should be as large as possible, while the filter length $L_{\min}$ should be small. The convexity of the optimization problem however decreases in these limits. We have found a set of parameters that facilitates a good compromise between acceptable approximation of the physics in solid and fluid areas as well as an objective found that is smooth with respect to variations of the design variables

$$L_{\min} = h_{\text{mesh}}, \quad \xi = 10, \quad q = 4 \cdot 10^{-6} \quad \text{and} \quad \text{Da} = \frac{\eta_s + \eta_p}{L^2 \alpha_{\max}} = 10^{-5}, \tag{11}$$

where the Darcy number Da has been introduced in terms of the characteristic length scale L. It describes the magnitude of viscous forces relative to damping forces in solid regions, and it thus belongs among the other numerical parameter. Should a design without a steady solution appear, we use the final transient solution to calculate the derivative of the objective function, ϕ. This gradient is used to improve the design in an iterative way using the method of moving asymptotes [17].

We find it convenient to introduce symmetry by defining

$$\theta_{\text{sym}} = (\theta + \theta(x, -y))/2, \tag{12}$$

and using θ_{sym} in place of θ in the PDE filter (8). Equation (12) is specific to a horizontal symmetry axis as used in the following section, but it is straight forward to generalize it to vertical or 180 degree rotational symmetry.

6. Cross with Horizontal Symmetry

The cross geometry is illustrated in figure 2 with a forced horizontal symmetry axis for the design, inlets to the sides and outlets in the upper and lower channels. The channel width L is chosen as characteristic length scale and the size of the design domain is taken as $L_d = 2L$. At a critical driving pressure the system goes through a pitchfork bifurcation as illustrated in figure 3.

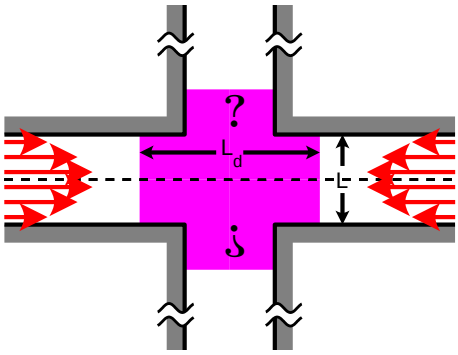

Figure 2: The setup for optimization of the symmetric cross is shown with inlets to the sides a central design domain. Note that the design is mirrored around the dashed symmetry line. The distance from the center to the inlet is $2L$, while it is $4L$ for the outlet. The flow is pressure driven with $\underline{\underline{\mathbf{A}}} = \underline{\mathbf{I}}$ at the inlets.

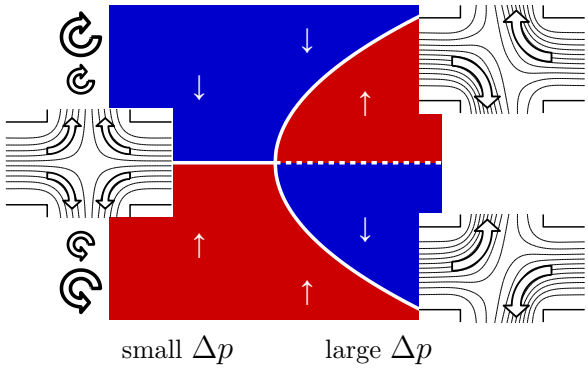

Figure 3: A pitchfork bifurcation is illustrated with rotation as solution variable on the y-axis. Red and blue areas represent areas with increasing clock- and counterclockwise rotation, respectively. The insets show the symmetric and two asymmetric solutions at their respective position in the diagram.

The system can be forced in the unstable symmetric solution by enforcing zero normal flow along the symmetry line, which gives rise to an increased hydraulic resistance and thus smaller dissipation as illustrated in figure 4. Note that the dissipation would be increasing in the case of a flow rate driven setup. The point of bistability appears implicitly in the solution, so it is not straightforward to optimize for this. We opt for a heuristic approach based on the dissipation ratio between the two states, i.e.

$$\phi = P_{\text{asym}}/P_{\text{sym}}$$

That is we hope to decrease the critical driving pressure by pulling apart the two curves in figure 4. We use the physical parameters of equation (7), and it now makes sense to remark that the relation between

the driving pressure and the characteristic pressure serves to put the average inlet velocity close to unity for the empty design, while $\beta = 0.2$ is an upper limit for the existence of bistability in the first place.

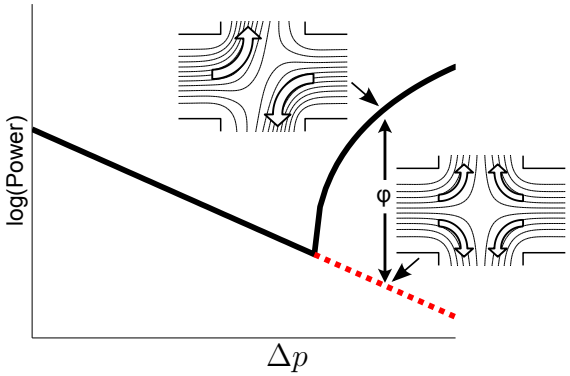

Figure 4: The logarithm of the power dissipation is sketched as a function of the driving pressure for the asymmetric (black) and symmetric flow solution (red). The distance between the two curves, ϕ is the ratio between the power dissipation in the two states. The purpose of choosing this ratio as objective function is that it tends to pull the curves apart, which indirectly moves the point of bistability to the left – assuming the slope of the curves is unaffected.

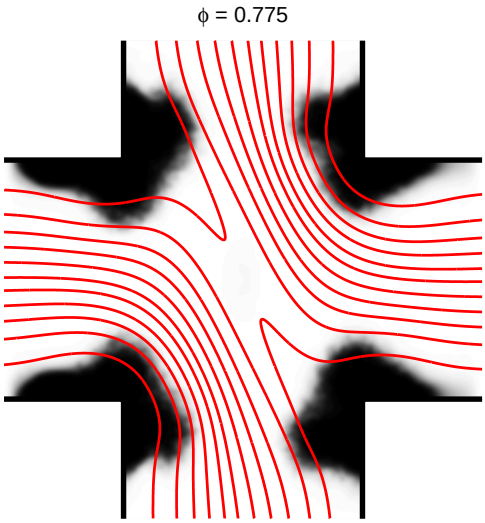

Figure 5: Topology optimization of the cross for maximum dissipation ratio gives rise to contractions in the corners.

Figure 5 shows the result of an optimization with these physical parameters and the numerical parameters of equation (11). It is not surprising that the optimization produces contractions, since this increases the effective We. The contractions keep growing as long as the shear rate* increases, but at some point the pressure driven nature of the system becomes active in the sense, that the flow rate begins to drop. It thus seems that the contraction width goes to zero for increasing length of the outlet channels.

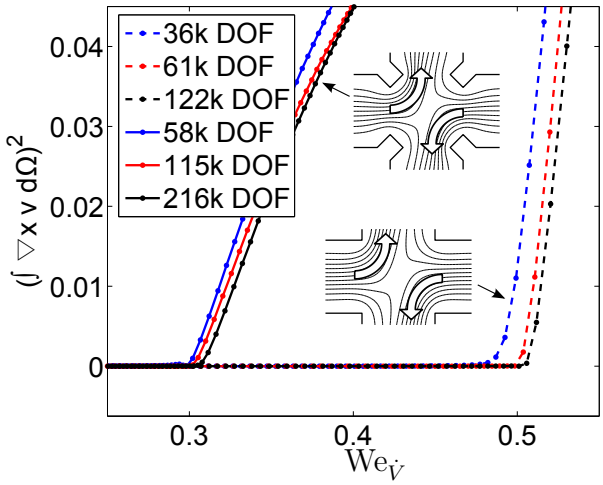

Figure 6: The integral of the vorticity is squared and plotted as a function of We for designs using different number of degrees of freedom (DOF). The simulations for the empty design (dashed lines) converge to indicate a point of bistability at $We_{\dot{V}} = 0.5$, while the simulations of the contraction design indicate a much smaller value although these results are not fully converged. The contraction design is produced by subtracting the small squares from the empty design. The squares are centered on the corners rotated 45 degrees and have side length of $L/4$.

*and thus the effective Weissenberg number

We perform simulations in a geometry inspired from the result of the optimization to verify that the working mechanism does not depend on the damping term in way that is not physical. Note that these simulations are performed by slowly ramping down We:

$$\mathrm{We} = \mathrm{We}_{\max} + \mathrm{st}(t)\,(\mathrm{We}_{\min} - \mathrm{We}_{\max}) \tag{13}$$

where $\mathrm{st}(t)$ is a regularized step function[†] with a width of $T_{\mathrm{step}} = 4000\mathrm{We}_{\max}(0.035L/h_{\mathrm{mesh}})$. We integrate the vorticity over the center of the domain for each We number, as we find that the square of this is a good measure of asymmetry. In figure 6 we thus plot this quantity versus We numbers, $\mathrm{We}_{\dot{V}}$, based on the flow rates for easier comparison with literature, but in fact no reference exists for the FENE-CR model[‡].

7. Cross with Vertical Symmetry, Two Fluids Simultaneously

In this section we consider the flow of two fluids with slightly different relaxations times meeting in a cross as illustrated in figure 7. Apart from a vertical symmetry axis and a design domain confined to the corners, the setup is identical the previous problem. We model the different relaxation times by convecting a marker field c,

$$\begin{aligned} \mathbf{v}\cdot\boldsymbol{\nabla} c &= 0, \ \text{in}\ \Omega, \quad c = 0 \ \text{at left inlet}, \quad \text{and} \quad c = 1 \ \text{at right inlet}, \\ \bar{c} &= \tfrac{1}{2} + \frac{\tanh(\xi_c(c-\tfrac{1}{2}))}{2\tanh(\xi_c/2)}, \quad \text{and} \quad \mathrm{We} = \mathrm{We}_{\mathrm{left}} + \bar{c}\,(\mathrm{We}_{\mathrm{right}} - \mathrm{We}_{\mathrm{left}}) \end{aligned}$$

where we choose $\xi_c = 4$, 1st order polynomials for c and SUPG stabilization for the convective equation. Our hypothesis is that an arbitrary design without a horizontal symmetry axis causes different dissipations for the two solutions in the manner illustrated in figure 9, which reflects the fact that one of the solutions has become disconnected from the solution at low pressure as illustrated in 8. We aim make the system favor the solution where the fluid coming from the with the smaller relaxation goes up (clockwise flow). This corresponds to maximizing the gap in figure 9, i.e.

$$\phi = P^{\circlearrowleft}_{\mathrm{asym}}/P^{\circlearrowleft}_{\mathrm{asym}}, \tag{14}$$

where $P^{\circlearrowleft}_{\mathrm{asym}}$ refers to dissipation for the solution with most of the flow coming from the left going up. That is we try to pull the curves in figure 9 apart.

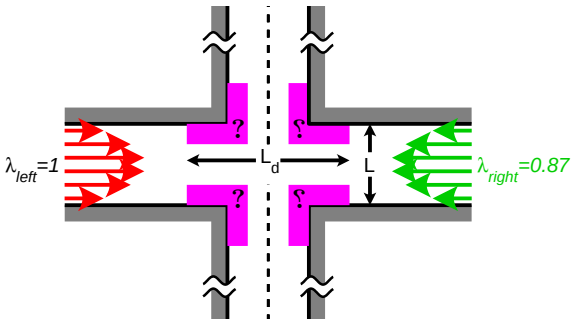

Figure 7: The setup for optimization where two fluids with different relaxation times meet in a cross. Note that the design domain is confined to the corners and mirrored around the dashed symmetry line. The distance from the center to the inlet is $2L$, while it is $4L$ for the outlet. The flow is pressure driven with $\underline{\underline{\mathbf{A}}} = \underline{\underline{\mathbf{I}}}$ at the inlets.

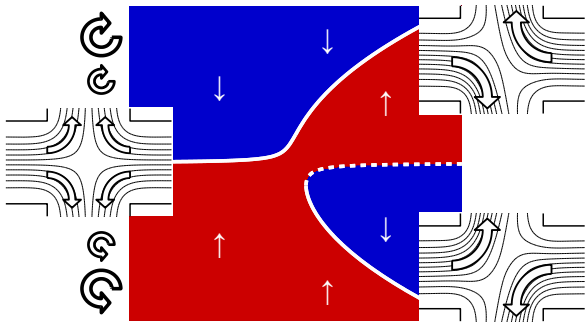

Figure 8: An asymmetric pitchfork bifurcation is illustrated with rotation as solution variable on the y-axis. Red and blue areas give rise to increasing clock- and counterclockwise rotation, respectively. The insets show the two asymmetric solutions at their respective position in the diagram.

In order to reliable compute both of the dissipations in the objective (14), we impose a time-dependent damping field listed in the appendix. The effect of this is that we start every simulation with a diagonal wall to establish one of the states, before slowly removing this wall and enforcing the actual design.

[†]We use a third order polynomial to construct the step function.

[‡]Based on personal correspondence with Manuel A. Alves, we believe [15] presents results for the FENE-MCR model.

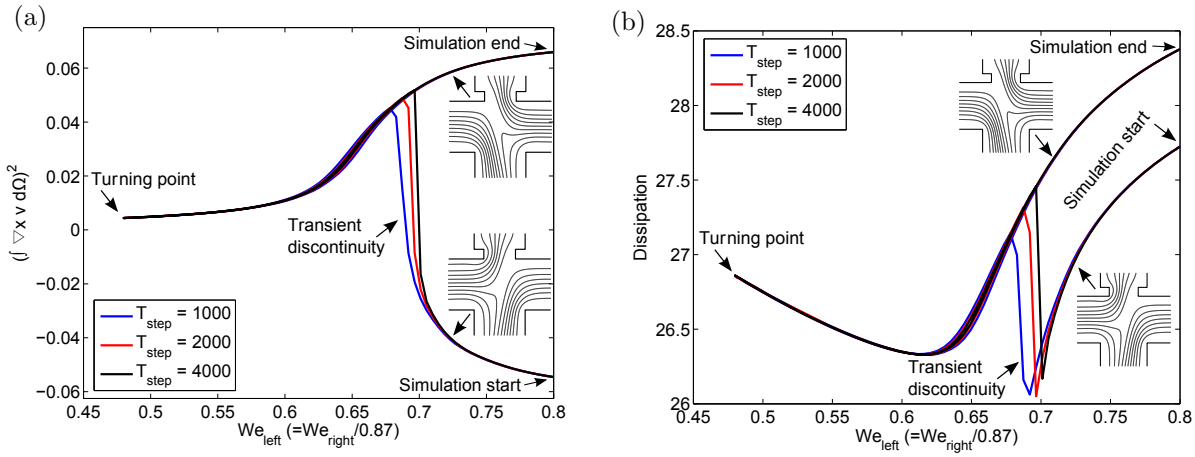

Figure 11: The squared integral of the vorticity (a) and the dissipation (b) are plotted as a function of $\mathrm{We}_{\mathrm{left}}$ for two different initial conditions (see insets). The simulation is initialized with a counter -clockwise rotation and it jumps to the other solution in as a transient discontinuity. That is the jump appears steeper as the simulation is performed slower. The contraction design is produced by subtracting the small squares from the empty design. The squares have a side length of $0.2L$ and 104 thousand degrees of freedom is used for each time step.

In terms of physical parameters we keep $\beta = 0.2$, $\alpha^2_{\mathrm{max}} = 100$, $\Delta p = 67.2 p_{\mathrm{char}}$, and set $\mathrm{We}_{\mathrm{left}} = 0.75$ and $\mathrm{We}_{\mathrm{right}} = 0.87\mathrm{We}_{\mathrm{left}}$. This results in a contraction in the upper outlet (see figure 9), which indicates that the larger dissipation is related to having the fluid with the longer relaxation time flowing through the contraction.

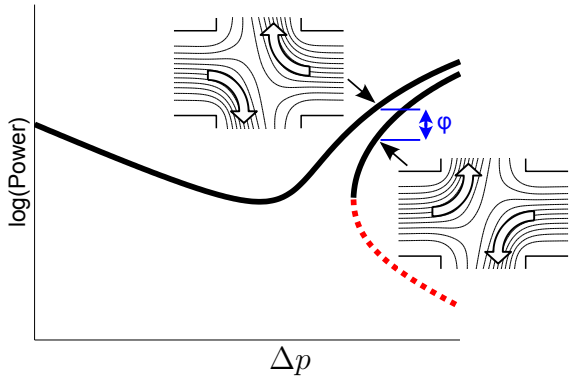

Figure 9: The logarithm of the power dissipation is sketched as a function of the driving pressure for the two asymmetric solutions. The distance between the two curves, ϕ is the ratio between the power dissipation in the two states.

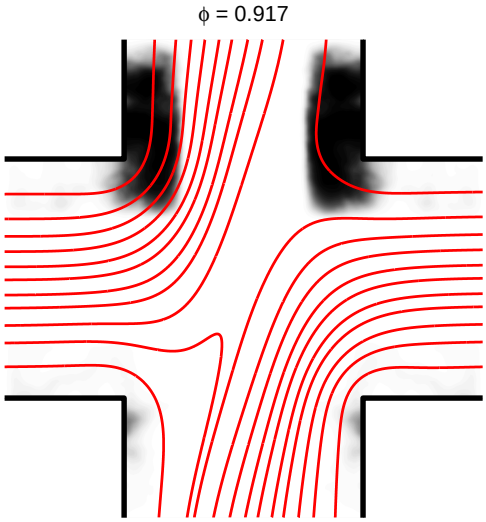

Figure 10: Topology optimization of the cross with two fluids for maximum dissipation ratio gives rise to a contraction at the upper outlet. Streamlines are only shown for the solution with the lower dissipation.

As shown in figure 11 we once again validate the result by performing simulations in a design inspired by the optimization. Note that these simulations are performed by starting from the state with counter clock-wise flow and slowly ramping down the pressure (both $\mathrm{We}_{\mathrm{left}}$ and $\mathrm{We}_{\mathrm{right}}$) similar to equation (13), before ramping it back up again such that the total simulation time becomes $2T_{\mathrm{step}}$. We see a transient discontinuity as predicted by figures 8 and 9, when we plot the squared integrated vorticity and dissipation in figures 11a 11b, respectively.

8. Cross with Rotational Symmetry, Two Fluids, not Simultaneously

Having confirmed that it is possible to use the dissipation ratio (14) to control the asymmetry of the viscoelastic flow in a cross, we now aim to make the asymmetry selective to the fluid flowing, i.e. the clockwise flow should be chosen $\beta = 0.15$, while the counterclockwise is chosen for $\beta = 0.2$ as illustrated in figure 12.

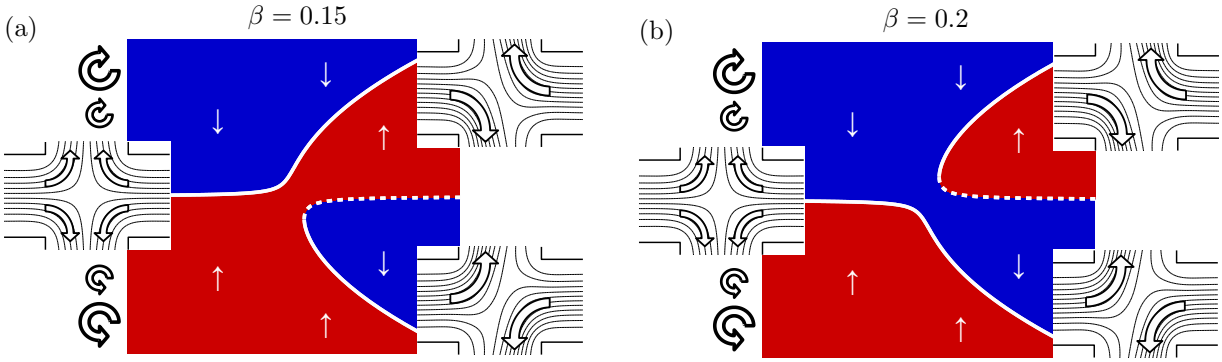

Figure 12: The idea of asymmetry selective to the fluid is presented. The geometry should select different asymmetric solutions depending on the whether $\beta = 0.15$ or $\beta = 0.2$.

We aim to achieve this by considering the dissipation as this approach was succesful for the previous example. This time we however minimize the larger of two objective functions,

$$\begin{aligned} \phi &= \max\left(\phi_{\beta=0.2}, \phi_{\beta=0.15}\right) \quad \text{where} \\ \phi_{\beta=0.2} &= P^{\circlearrowleft}_{\beta=0.2}/P^{\circlearrowleft}_{\beta=0.2} \quad \text{and} \quad \phi_{\beta=0.15} = P^{\circlearrowleft}_{\beta=0.15}/P^{\circlearrowleft}_{\beta=0.15}. \end{aligned} \tag{15}$$

We assume that the favored flow solution has the bigger dissipation, because it means that decreasing both objective functions below unity, yields the desired effect. This approach requires that we simulate the flow of a fluid with a solvent to total viscosity ratio of $\beta = 0.2$ and then $\beta = 0.15$. We furthermore compute the dissipation for both the clockwise and counterclockwise flow using the time varying damping field listed in the appendix, such that each optimization iteration considers four flow solutions[§]. Apart from the identical flow relaxation times and a design with 180 degree rotational symmetry, the setup is identical to that illustrated in figure 7. For the physical parameters we keep $\mathrm{We} = 0.75$ and $a^2_{\max} = 100$, but we increase the distance between the center and the outlet to $8L$ and set $\Delta p = 112 p_{\mathrm{char}}$ to compensate for the increased resistance.

The gradients of the objective functions $\phi_{\beta=0.2}$ and $\phi_{\beta=0.15}$ are highly anti parallel, and we have only been able to improve on the initial highly symmetric design by employing the globally convergent version of the method of moving asymptotes [18]. We use a mesh with horizontal as well as vertical symmetry, and we find that we are in many cases able to compute the flow for a new design, θ_{new} from the flow in and old design, θ_{old} using a continuation approach, i.e.

$$\theta = \theta_{\mathrm{old}}(1 - c_\theta) + \theta_{\mathrm{new}} c_\theta, \tag{16}$$

where c_θ is the continuation parameter starting from 0 and going to 1. It is only when this continuation fails, that we have to resort to transient simulations. Figure 13 represents the current status on this optimization problem. The objective functions do not deviate less from unity than those presented in the previous examples, although one would expect this, considering the difficulty of the problem. The design is supposed to favor the clockwise flow for $\beta = 0.15$, where the fluid is squeezed slightly less by the contractions as compared to the counterclockwise flow. Presently we have not been able to validate this result using a hard wall simulation and a geometry inspired by the optimization.

[§] We always perform the flow simulations in parallel.

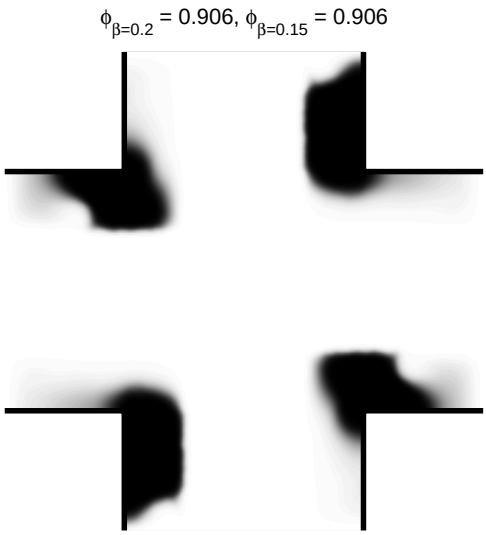

Figure 13: Topology optimization of the cross for asymmetry selective to the fluid is shown with contractions from the inlets going in to the center at upper right and lower left corners, while the contractions in the outlets occur at the upper right and lower left.

Conclusion
We have been able to optimize the viscoelastic flow in a cross for early bistability. We furthermore established and confirmed a hypothesis related to the dissipation in an asymmetric cross, when two fluids with different relaxation times are flowing from the inlets. Finally we presented some preliminary results on asymmetric flow selective to the fluid. All of these results are based on heuristic objective functions rather than a strict analysis at the point of bistability.

Acknowledgment
The presentation of this work at WCSMO10 is supported by the foundation of Fabrikant P. A. Fisker.

1 References

References

[1] P.E. Arratia, CC Thomas, J. Diorio, and JP Gollub. Elastic instabilities of polymer solutions in cross-channel flow. *Physical review letters*, 96(14):144502, 2006.

[2] F. Baaijens, S.H.A. Selen, H.P.W. Baaijens, G.W.M. Peters, and H.E.H. Meijer. Viscoelastic flow past a confined cylinder of a low density polyethylene melt. *Journal of Non-Newtonian Fluid Mechanics*, 68(2-3):173–203, 1997.

[3] RB Bird, PJ Dotson, and NL Johnson. Polymer solution rheology based on a finitely extensible bead–spring chain model. *Journal of Non-Newtonian Fluid Mechanics*, 7(2-3):213–235, 1980.

[4] T. Borrvall and J. Petersson. Topology optimization of fluids in Stokes flow. *International Journal for Numerical Methods in Fluids*, 41(1):77–107, 2003.

[5] L. Carracciuolo, D. Casaburi, L. D'Amore, G. D'Avino, PL Maffettone, and A. Murli. Computational simulations of 3d large-scale time-dependent viscoelastic flows in high performance computing environment. *Journal of Non-Newtonian Fluid Mechanics*, 166:1382–1395, 2011.

[6] MD Chilcott and JM Rallison. Creeping flow of dilute polymer solutions past cylinders and spheres. *Journal of Non-Newtonian Fluid Mechanics*, 29:381–432, 1988.

[7] K. Ejlebjerg Jensen, P. Szabo, and F. Okkels. Topology optimization of viscoelastic rectifiers. *Applied Physics Letters*, 100(23):234102–234102, 2012.

[8] R. Fattal and R. Kupferman. Time-dependent simulation of viscoelastic flows at high weissenberg number using the log-conformation representation. *Journal of Non-Newtonian Fluid Mechanics*, 126(1):23–37, 2005.

[9] A. Fortin, R. Guenétte, and R. Pierre. On the discrete evss method. *Computer Methods in Applied Mechanics and Engineering*, 189(1):121–139, 2000.

[10] A. Groisman, M. Enzelberger, and S.R. Quake. Microfluidic memory and control devices. *Science*, 300(5621):955, 2003.

[11] K. Ejlebjerg Jensen, P. Szabo, F. Okkels, and MA Alves. Experimental characterisation of a novel viscoelastic rectifier design. *Biomicrofluidics*, 6:044112, 2012.

[12] BS Lazarov and O. Sigmund. Filters in topology optimization based on helmholtz-type differential equations. *International Journal for Numerical Methods in Engineering*, 86(6):765–781, 2011.

[13] L.H. Olesen, F. Okkels, and H. Bruus. A high-level programming-language implementation of topology optimization applied to steady-state Navier-Stokes flow. *International Journal for Numerical Methods in Engineering*, 65(7):975–1001, 2006.

[14] RJ Poole, MA Alves, and PJ Oliveira. Purely elastic flow asymmetries. *Physical review letters*, 99(16):164503, 2007.

[15] Gerardo N Rocha, Robert J Poole, Manuel A Alves, and Paulo J Oliveira. On extensibility effects in the cross-slot flow bifurcation. *Journal of Non-Newtonian Fluid Mechanics*, 156(1):58–69, 2009.

[16] M. Sahin. Parallel large-scale simulation of viscoelastic fluid flow instabilities. In *17th International Workshop on Numerical Methods for Non-Newtonian Flows*, 2012.

[17] K. Svanberg. The method of moving asymptotes-a new method for structural optimization. *International Journal for Numerical Methods in Engineering*, 24(2):359–373, 1987.

[18] Krister Svanberg. A class of globally convergent optimization methods based on conservative convex separable approximations. *SIAM Journal on Optimization*, 12(2):555–573, 2002.

[19] F. Wang, B.S. Lazarov, and O. Sigmund. On projection methods, convergence and robust formulations in topology optimization. *Structural and Multidisciplinary Optimization*, 43(1):767–784, 2011.

Appendix

In order to reliable compute both of the dissipations in the objective (14), we impose a time-dependent damping field,

$$\alpha = \begin{cases} \alpha_0 & , \quad t < 10\mathrm{We}_{\mathrm{left}} \\ \alpha_0[t/(10\mathrm{We}_{\mathrm{left}}) - 2]^2 & , 10\mathrm{We}_{\mathrm{left}} \leq \ t < 20\mathrm{We}_{\mathrm{left}} \\ \alpha_D[t/(10\mathrm{We}_{\mathrm{left}}) - 2]^2 & , 20\mathrm{We}_{\mathrm{left}} \leq \ t < 30\mathrm{We}_{\mathrm{left}} \\ \alpha_D & , 30\mathrm{We}_{\mathrm{left}} \leq \ t \end{cases}, \quad \text{where} \tag{17}$$

$$\alpha_0 = \begin{cases} \alpha_{\max} & , |x| < 1 \ \& \ |y| < 1 \ \& \ y - 0.2 < x < y + 0.2 \\ 0 & , \text{otherwise} \end{cases}, \quad \text{for } P^{\circlearrowleft}_{\mathrm{asym}} \text{ and}$$

$$\alpha_0 = \begin{cases} \alpha_{\max} & , |x| < 1 \ \& \ |y| < 1 \ \& \ -y - 0.2 < x < -y + 0.2 \\ 0 & , \text{otherwise} \end{cases}, \quad \text{for } P^{\circlearrowleft}_{\mathrm{asym}}$$

that is we start every simulation with a diagonal wall to establish one of the states, before slowly removing this wall and enforcing the actual design, α_D given by the right-hand side of equation (10).